


# Wearable Multifunctional Health Monitoring Systems Enabled by Ultrafast Flash-Induced 3D Porous Graphene


Se Jin Choi, Chan Hyeok Kim, Jeong Hyeon Kim, Kang Hyeon Kim, Sang Yoon Park, Yu Jin Ko, Hosung Kang, Young Bin Kim, Yu Mi Woo, Jae Young Seok, Bongchul Kang, Chang Kyu Jeong, Kwi-Il Park, Geon-Tae Hwang, Jung Hwan Park\*, and Han Eol Lee\* 

A wearable health monitoring system is a promising device for opening the era of the fourth industrial revolution due to increasing interest in health among modern people. Wearable health monitoring systems were demonstrated by several researchers, but still have critical issues of low performance, inefficient and complex fabrication processes. Here, we present the world's first wearable multifunctional health monitoring system based on flash-induced porous graphene (FPG). FPG was efficiently synthesized via flash lamp, resulting in a large area in four milliseconds. Moreover, to demonstrate the sensing performance of FPG, a wearable multifunctional health monitoring system was fabricated onto a single substrate. A carbon nanotube-polydimethylsiloxane (CNT-PDMS) nanocomposite electrode was successfully formed on the uneven FPG surface using screen printing. The performance of the FPG-based wearable multifunctional health monitoring system was enhanced by the large surface area of the 3D-porous structure FPG. Finally, the FPG-based wearable multifunctional health monitoring system effectively detected motion, skin temperature, and sweat with a strain GF of 2564.38, a linear thermal response of  $0.98 \Omega^{\circ}\text{C}^{-1}$  under the skin temperature range, and a low ion detection limit of  $10 \mu\text{M}$ .

## 1. Introduction

With the emergence of the hyperconnected era, Internet of Things (IoT) devices have been developed to collect data on environmental changes and user conditions in real-time, enabling to apply to various practical applications such as smart homes/farms, automation factories, and remote patient monitoring.<sup>[1–3]</sup> Especially, wearable health monitoring sensors have been considered an attractive candidate for next-generation IoT devices to continuously measure bio-signal changes due to their light-weight, body attachability, and versatility.<sup>[4,5]</sup> Although various thin-film-based wearable sensors with Si, compound semiconductors, and complex oxides have been investigated by several researchers, they have some structural and process limitations to realizing the high-performance devices such as low surface area, inefficient manufacturing, and high-temperature procedures.<sup>[6,7]</sup>

S. J. Choi, J. H. Kim, K. H. Kim, S. Y. Park, Y. J. Ko, Prof. C. K. Jeong, Prof. H. E. Lee  
Department of JBNU-KIST Industry-Academia Convergence Research, Jeonbuk National University, 567 Baekje-daero, Deokjin-gu, Jeonju-si, Jeollabuk-do 54896, Korea  
Division of Advanced Materials Engineering, Jeonbuk National University, 567 Baekje-daero, Deokjin-gu, Jeonju-si, Jeollabuk-do 54896, Korea  
Division of Electronics and Information Engineering, Jeonbuk National University, 567 Baekje-daero, Deokjin-gu, Jeonju-si, Jeollabuk-do 54896, Korea  
E-mail: haneol@jbnu.ac.kr  
C. H. Kim  
School of Mechanical System Engineering, Kumoh National Institute of Technology, 61 Daehak-ro, Gumi, Gyeongbuk 39177, Korea  
Dr. H. Kang  
Institute of Battery R&D, LG Energy Solution, 118, Munji-ro, Daejeon 34122, Korea  
Department of Biological and Environmental Engineering, Cornell University, 111 Wing Dr, Ithaca, New York 14853, USA  
Y. B. Kim  
Department of Materials Science and Engineering, Korea Advanced Institute of Science and Technology (KAIST), 291 Daehak-Ro, Yuseong-Gu, Daejeon 34141, Korea

Y. M. Woo, Prof. J. H. Park  
Department of Mechanical Engineering (Department of Aeronautics, Mechanical and Electronic Convergence Engineering), Kumoh National Institute of Technology, 61 Daehak-Ro, Gumi, Gyeongbuk 39177, Korea  
E-mail: parkjh1151@kumoh.ac.kr  
Prof. J. Y. Seok  
Department of Mechanical System Design Engineering, Seoul National University of Science and Technology, 232 Gongneung-ro, Nowon-gu, Seoul 01811, Korea  
Prof. B. Kang  
School of Mechanical Engineering, Kookmin University, 77 Jeongneung-ro, Seongbuk-gu, Seoul 02707, Korea  
Prof. K.-I. Park  
Department of Materials Science and Metallurgical Engineering, Kyungpook National University, 80 Daehak-ro, Buk-gu, Daegu 41566, Korea  
Prof. G.-T. Hwang  
Department of Materials Science and Engineering, Pukyong National University, 45 Yongso-ro, Nam-Gu, Busan, 48513, Korea  
 The ORCID identification number(s) for the author(s) of this article can be found under https://doi.org/10.1002/eem2.70005.

DOI: 10.1002/eem2.70005

Porous graphene has attracted attention as a promising active layer of wearable devices, due to its lightweight, permeability, excellent electrical properties, and large surface area.<sup>[8–13]</sup> Nevertheless, previously reported porous graphene has critical issues of expensive, inefficient, and complex fabrication processes.<sup>[14–16]</sup> Recently, light-polymer interaction has been proposed to form porous graphene film owing to the simple fabrication process, micro-processability, and ease of forming the desired pattern.<sup>[17]</sup> However, conventional laser-induced graphene fabrication is unsuitable for massive and rapid production because of its limited processing area, slow/expensive process, and high-energy light dependence.<sup>[18–20]</sup> According to the necessity of a low-cost and scalable photo-reactive process, the flashlight is regarded as an emerging light source to realize porous graphene film since the flash has the advantages of ultrashort radiation time ( $\sim$ ms), large-scale processability ( $>5 \times 10 \text{ cm}^2$  by one flash shot), and high energetic efficiency.<sup>[21]</sup> Despite these excellent characteristics of the flashlight, which has a wide wavelength range and large irradiation area, has an inherent limitation for precisely controlling the pore size/shape, density, and arrangement of the porous graphene, making it difficult to apply electronic devices requiring specific characteristics. To solve this issue, in-depth analysis of the flashlight-material reaction mechanism is required to enable precise control of photo-process parameters with various degrees of freedom.<sup>[22]</sup>

Electrode formation onto the porous structure surface has been recognized as a significant obstacle to realizing wearable devices.<sup>[23–27]</sup> The conventional physical deposition including sputtering, thermal evaporation, electron beam evaporation, and pulsed laser deposition hardly forms metal thin-film electrodes owing to their poor step coverage, low adhesion force, and cracking.<sup>[28]</sup> Although several electrode-forming technologies with nanocomposite (e.g., 3D-printing, electrospinning, sol-gel method) have been suggested to resolve these issues, some assignments for commercialization still remained such as high resolution, large-scale/rapid process, and applicability of diverse materials.<sup>[29–34]</sup> Screen printing method is conceded as a potential method for making large-scale electrodes onto the porous structure since it can rapidly provide the desired large-scale patterns using a metal shadow mask.<sup>[35–37]</sup> In addition, this method allows the realization of thin electronic devices on uneven/rough material surfaces without any defects by modifying the electrode dimension.<sup>[38,39]</sup>

Herein, we report the first wearable multifunctional health monitoring systems via ultrafast flash-induced three-dimensional porous graphene (FPG). Upon an initial flash exposure, the surface of a conventional polyimide (PI) film rapidly transformed into the FPG within 3 ms via various synergistic photothermal reactions, including PI decomposition, carbonization, graphenization, and subsequent gas expulsion. The porosity of the FPG structures could be further maximized by irradiating additional flashlight because the gaseous byproducts generated from light-polymer interaction explosively released through numerous FPG pore channels, expanding its 38.58% porous network and 726% surface area. The developed FPG process enabled the generation of large-scale ( $5 \times 10 \text{ cm}^2$ ) patterned (e.g., circle and rectangle) FPG on the PI surface by introducing a shading mask during the flash lamp process, which ensured scalability and adaptability of the FPG formation process for customized technological applications. In addition, two successive shots of the flash lamp enhanced the electrical conductivity of the FPG via additional carbonization/graphenization reactions and defect annihilation, resulting in 31.37% improvement of FPG sheet resistance compared to that of FPG formed by initial flash irradiation. The flash energy fluence and shot number effects to the

FPG morphology and quality were analyzed using various characterization tools, including scanning electron microscopy (SEM), computer-aided vision image analysis, Raman spectroscopy, X-ray photoelectron spectroscopy (XPS), and Fourier transform infrared spectroscopy (FT-IR). The theoretical basis of the FPG methodology was thoroughly verified by 3D transient photothermal calculations based on finite element analysis. Flexible electrodes on the uneven FPG surface were accomplished by the simple screen printing process of carbon nanotube-polydimethylsiloxane (CNT-PDMS) nanocomposite ink. The FPG-based flexible biomedical sensors were constructed to measure joint strain, skin temperature, and sweat ions ( $\text{K}^+$  and  $\text{Cl}^-$ ). Finally, a wearable multifunctional sensing system was successfully realized in a single substrate for monitoring the change of biosignals in real time.

## 2. Results and Discussion

**Figure 1a** displays a 3D schematic illustration of wearable health monitoring sensors, performed by ultrafast flash-polymer interaction and large-scale screen printing process. The detailed procedure is as follows: i) The pulsed flashlight with a broad spectrum (wavelength from 200 to 1000 nm) was exposed to a polyimide (PI) substrate within a few milliseconds, leading to a highly efficient conversion of the PI surface into the porous graphene via rapid PI decomposition and subsequent release of gaseous byproducts (e.g., carbon dioxide [ $\text{CO}_2$ ] and nitrogen [ $\text{N}_2$ ]); ii) CNT-PDMS nanocomposite-based electrodes were screen printed onto the uneven/rough surface of the FPG. Prior to the printing, the 3 wt% CNT powder was mixed with PDMS, and subsequently stirred during 60 min to make CNT-PDMS nanocomposite ink. The customized stainless mask was aligned on the FPG and then spread the poured CNT-PDMS ink by moving a printing head with  $50 \text{ mm s}^{-1}$ . After thermal curing for 1 h at  $80^\circ\text{C}$ ,  $100 \mu\text{m}$ -thick electrode for each sensor could be made at a desired position by detaching the shadow mask. Ionophore-based membrane, which can selectively penetrate specific ions from top to bottom side, was coated onto the surface of the electrode/FPG structure for realizing ion sensors; and iii) Since the aforementioned processes of flashlight irradiation and screen printing were enabled to fulfill with large scale with the desired pattern shape, various sensors for measuring  $\text{K}^+$  ion,  $\text{Cl}^-$  ion, mechanical stress, and temperature were simultaneously manufactured onto a single PI film for achieving wearable multifunctional sensor systems. The detailed fabrication process is described in **Figure S1**, Supporting Information.

The developed FPG method enabled the formation of either large area or patterned graphene on the surface of a PI substrate, as presented in **Figure 1b**. The broad-area emission capability of the flash lamp effectively facilitated the transformation of the PI film into homogeneous graphene across a substantial surface area measuring  $3 \times 3 \text{ cm}^2$ . This conversion was achieved through a single flash irradiation, which ensured the uniform and scalable capability of the flashlight-polymer interaction for FPG synthesis. We believe that the scalability of the FPG process can be further enhanced by optimizing the reflector design of the flash lamp to ensure uniform irradiation across the substrate as well as minimizing the overlapped area during seamless processing for large-scale production. In addition, the selective FPG pattern, precisely aligning with the designated locations for the sensor array, was demonstrated by employing a shadow mask during the flash irradiation process. This adaptability allows for the fabrication of customized FPG structures with high spatial accuracy, meeting the requirements of

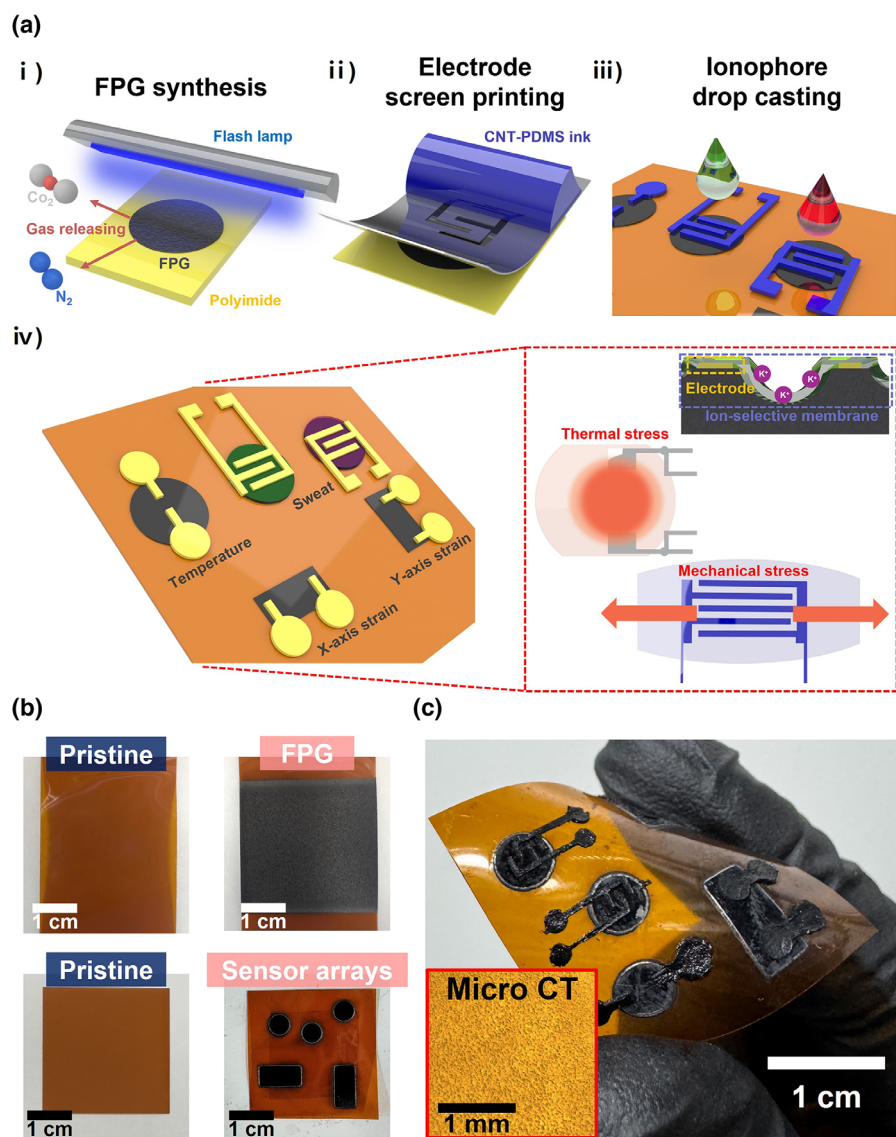


**Figure 1.** a) Schematic illustration of (i) FPG synthesis, (ii) fabrication process of CNT-PDMS nanocomposite electrode via screen printing, (iii) ionophore drop casting on FPG, and (iv) signal detection mechanism. b) Photographs of pristine PI and FPG on PI film, producing FPG layers with various shapes onto the desired locations. c) Optical image of flexible multifunctional sensor. The inset is a micro-CT image of FPG surface, showing its porous structure.

specific technological applications. Figure 1c presents the bent multifunctional sensor system with ion, strain, and temperature sensors. Resistive-type sensors for evaluating vertical/horizontal mechanical strain, and temperature were simply fabricated by the structure of the CNT-PDMS electrodes on rectangle-shaped FPGs ( $10 \times 5 \text{ mm}^2$  size), and circle-shaped FPG (diameter of 5 mm), respectively. In the case of  $\text{K}^+$  and  $\text{Cl}^-$  ion sensors, the interdigitated electrodes (IDEs) were formed onto the circular graphene to enhance the carrier collection efficiency.<sup>[40]</sup> The inset shows a micro-computed tomography (micro-CT) image of the FPG surface, indicating high numerous micropores in  $2 \times 2 \text{ mm}^2$ .

Figure 2a schematically illustrates the formation mechanisms of the FPG structures generated under the first and second flash lamp

exposures. The PI film temperature rapidly increased up to approximately  $1700^\circ\text{C}$  upon an initial flash exposure, causing fundamental transformation of the PI via combinatorial photothermal reactions, including dissociation of PI bonds ( $\text{C}=\text{O}$ ,  $\text{C}-\text{N}$ , and  $\text{C}-\text{O}$  bonds), carbonization, and graphenization.<sup>[41–44]</sup> The generated  $\text{CO}_2$ ,  $\text{N}_2$ , and  $\text{CO}$  gases during bond decomposition were expelled through the carbon structures, resulting in the creation of the FPG. Under the second flashlight irradiation, photon energy absorbed by the FPG/PI film enabled the formation of the FPG with significantly increased porosity by expanding its porous network. The porosity enhancement effect by the sequential flash exposure could be induced because the gaseous byproducts produced from further FPG formation actively released via numerous FPG pores, which served as channels for the efficient expulsion. Such structural evolution of the FPG enabled by additional flash lamp processing proposes that consecutive flash lamp treatments can be employed to achieve highly porous FPG structure for applications requiring high surface area and tailored porosity. To establish a theoretical basis for the FPG formation, 3D transient photothermal simulation was carried out based on the finite element method, as shown in Figure 2b. As the fluence of the pulsed flashlight increased to  $22 \text{ J cm}^{-2}$ , the flash-induced maximum temperature reached to  $\sim 1875^\circ\text{C}$  within the pulse width of 3 ms, which was sufficient to facilitate the formation of graphene.<sup>[41,42]</sup> Figure 2c presents the photographic images of PI films exposed under a flashlight (pulse width of 3 ms) with different energy densities ranging from 10 to  $22 \text{ J cm}^{-2}$ . The surface of the PI substrate slightly transformed into a carbonaceous layer at the flashlight fluence of  $10 \text{ J cm}^{-2}$  because the irradiated photon energy could raise the temperature of the PI up to approximately  $856^\circ\text{C}$  and

subsequently induce a carbonization reaction.<sup>[43,44]</sup> Upon the exposure of a flashlight with energy density of  $22 \text{ J cm}^{-2}$ , a dark black carbon layer was observed, which could be formed on the PI surface via combinatorial photothermal effects, including carbonization and graphenization.

Figure 2d shows the SEM images illustrating the surface morphology of PI films subjected to various flash lamp processing parameters (pulse duration was fixed to 3 ms), including flashlight energy densities and the number of applied pulses, to comprehensively investigate their effects on FPG structural evolution. A flashlight fluence of  $14 \text{ J cm}^{-2}$  triggered the breakdown of complex PI molecular chains through a carbonization reaction, leaving behind a melted PI surface with disordered carbon-rich residue. Upon irradiation with a flashlight energy density



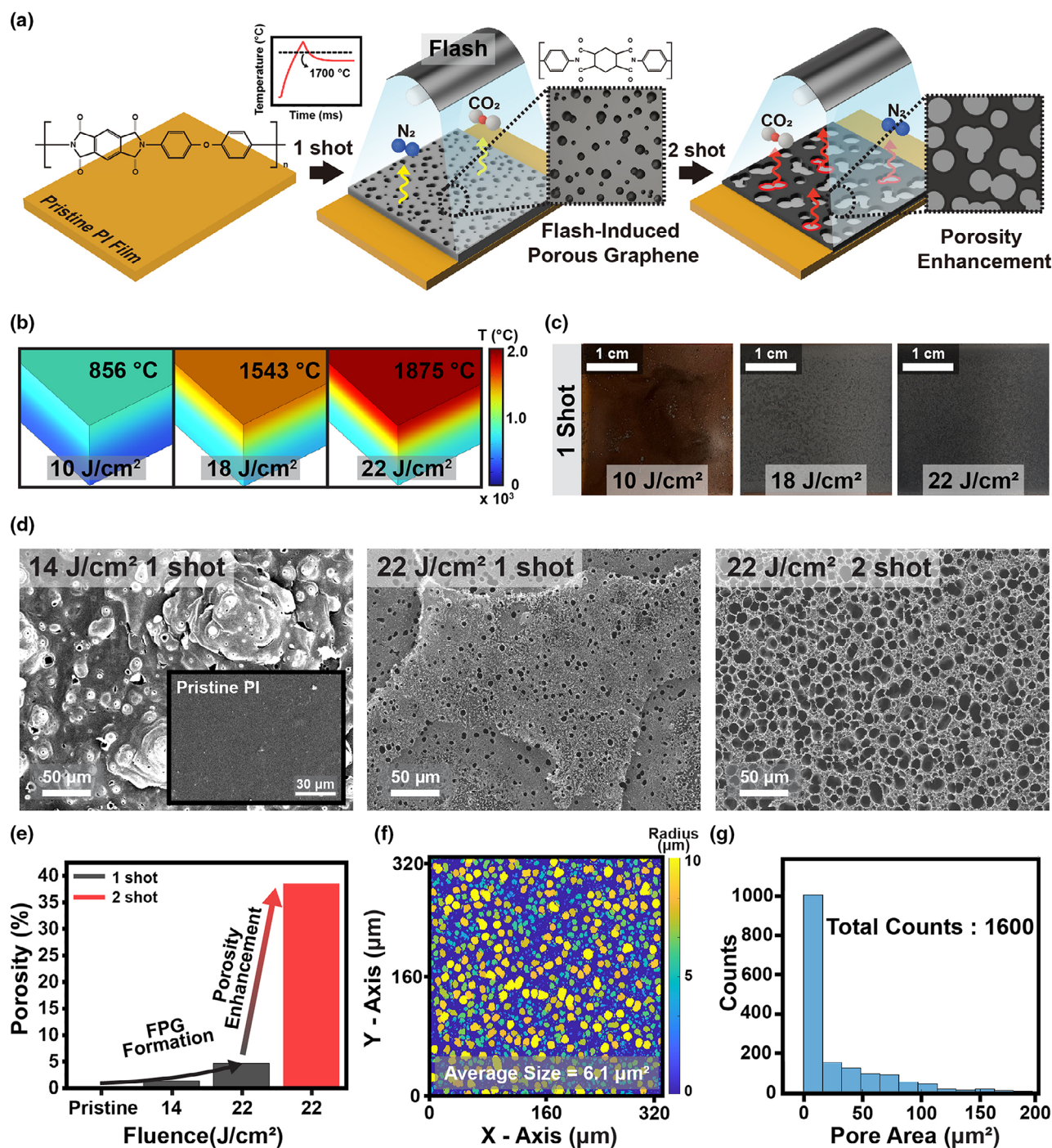


**Figure 2.** Fabrication process and structural characterization of FPG. a) Schematic illustration of FPG formation enabled by successive flashlight irradiation, b) Temperature distribution of PI simulated by COMSOL under flash fluence of 10, 18,  $22 \text{ J cm}^{-2}$ , c) FPG synthesized under flash energy densities of 10, 18,  $22 \text{ J cm}^{-2}$ , d) SEM images of FPG generated under first (at 14 and  $22 \text{ J cm}^{-2}$ ) and second (at  $22 \text{ J cm}^{-2}$ ) flashlight exposures, e) Porosity of pristine PI, and FPGs synthesized upon first (at 14 and  $22 \text{ J cm}^{-2}$ ) and second (at  $22 \text{ J cm}^{-2}$ ) flash lamp processes, f) Pore size distribution of the optimized FPG obtained by consecutive two shots of flash fluence at  $22 \text{ J cm}^{-2}$ , g) Quantitative pore size distribution of the optimized FPG (twice exposures at  $22 \text{ J cm}^{-2}$ ).

of  $22 \text{ J cm}^{-2}$ , the FPG structure emerged on the PI surface due to the carbonization and subsequent graphenization process. This transformation suggested that the high flashlight fluence not only initiated the decomposition of the PI into carbonaceous residues but also promoted

the rearrangement of these carbon atoms to facilitate the FPG formation with graphitic domains. At the consecutive flash lamp exposures (energy density:  $22 \text{ J cm}^{-2}$ , and number of pulses: twice), the surface morphology of the created FPG exhibited a higher density of



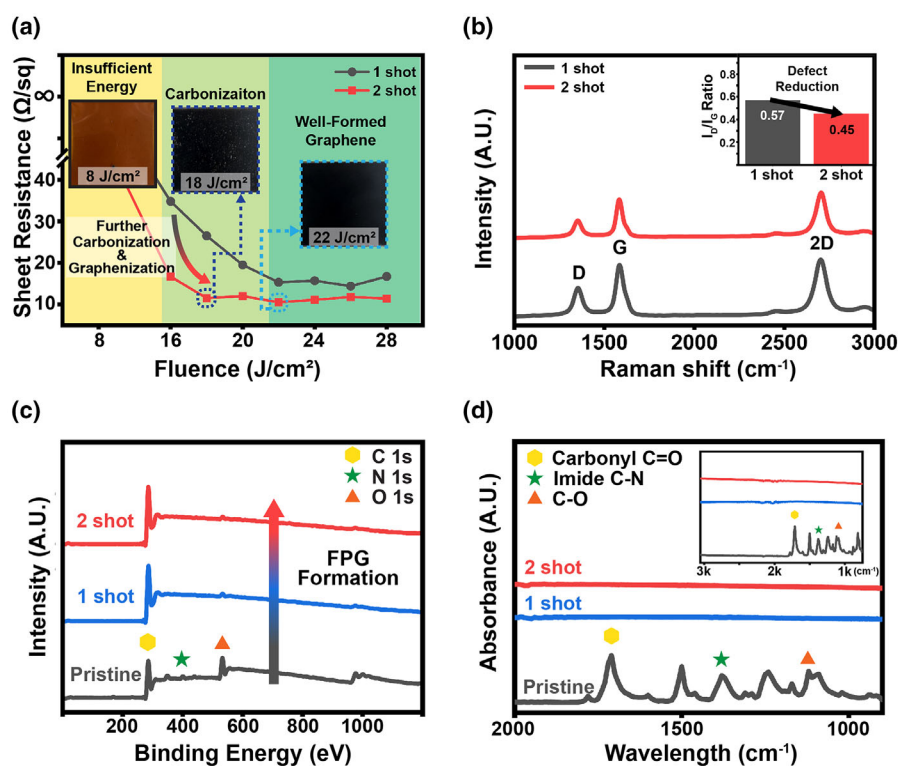


**Figure 3.** Physicochemical properties of FPG. a) Sheet resistance of FPG as a function of flash fluence (from 12 to 28  $\text{J}/\text{cm}^2$ ), and the number of irradiations (single and double), b) Raman spectra of FPG formed by single and twice exposure of flashlight with the energy density of 22  $\text{J}/\text{cm}^2$ . Inset shows  $I_D/I_G$  ratio of the corresponding FPGs, c) XPS spectra of pristine PI, and FPG processed by single and double exposure of flashlight with 22  $\text{J}/\text{cm}^2$  fluence, d) FT-IR spectra of pristine PI, and FPG upon first and second (at 22  $\text{J}/\text{cm}^2$ ) flash lamp processes.

interconnected voids. Such FPG structure with enlarged porosity and surface area was more beneficial to enhance material's flexibility and improve the electrochemical or adsorption capabilities for realizing wearable multifunctional sensors that can monitor a variety of bio-signals, including strain, temperature, and sweat ions. It was noteworthy that an additional third shot of the flashlight caused severe cracks within the FPG matrix due to the internal thermal and mechanical stresses accumulated during the repeated flash lamp process (Figure S2, Supporting Information). These cracks disrupt the continuity of the material, which is detrimental to the mechanical stability, and functional performance. Considering this critical threshold for the number of applied flash pulses, the flash lamp exposure was optimized to two pulses for the morphology and structural integrity of FPG. Figure 2e presents the porosity of the FPG fabricated by different flash lamp processing conditions. The porosity was obtained using computer-aided vision image analysis, which enabled precise quantification of the FPG's void structure. As the energy density of a single pulsed flashlight increased from 0 to 22  $\text{J}/\text{cm}^2$ , the porosity of the FPG was correspondingly enhanced from 0 to 4.67%, indicating a direct correlation between energy input and pore generation during the FPG formation. Under the application of two flash pulses at an energy fluence of 22  $\text{J}/\text{cm}^2$ , the porosity of the FPG increased substantially to 38.58%. This enhancement in porosity contributed to increased structural adaptability and flexibility of the FPG by facilitating the formation of a highly interconnected graphitic network. In addition, the resulting surface area

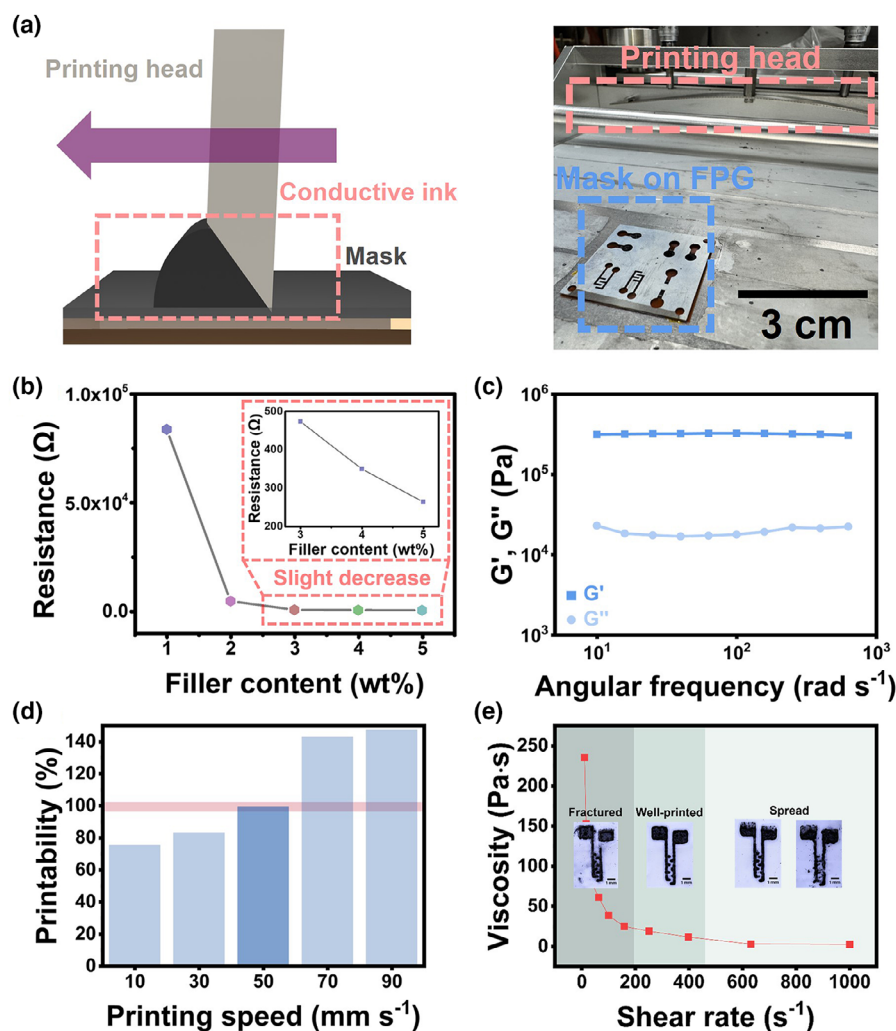
of 41917.5  $\mu\text{m}^2$ , measured within a total characterization area of 108643.8  $\mu\text{m}^2$ , was 726% higher than that of the FPG produced with a single flash pulse at an energy density of 22  $\text{J}/\text{cm}^2$ , which provided a significant advantage to improve performance of sensing applications that require high surface-to-volume ratios. Notably, among all flash lamp irradiation conditions performed for optimization, the application of two flash pulses at a fluence of 22  $\text{J}/\text{cm}^2$  resulted in the maximum porosity and pore area within the FPG structure (Figure S3, Supporting Information).

Figure 2f graphically illustrates the pore size distribution of the optimized FPG, revealing uniformly distributed voids with radii ranging from several micrometers to 10  $\mu\text{m}$  across the entire analyzed region (average pore size: 6.1  $\mu\text{m}^2$ ). According to the statistical data for the area of the FPG pores, approximately 62% of the voids in the optimized FPG exhibited pore area below 17  $\mu\text{m}^2$ . Such a controlled degree of uniformity in pore size was beneficial for achieving consistent material property and stability while simultaneously increasing the effective surface area and mechanical flexibility.

Two consecutive shots of the flash lamp not only increased the porosity of the FPG but also enhanced its electrical conductivity through further carbonization and graphenization processes. Figure 3a shows the sheet

resistance of the FPG demonstrated by various flash lamp processing parameters (pulse width was fixed to 3 ms), including energy densities and numbers of applied pulses. As the fluence of a single flash pulse increased up to 28  $\text{J}/\text{cm}^2$ , the sheet resistance decreased and eventually saturated down to approximately 15  $\Omega \text{ sq}^{-1}$ , attributable to the combined effects of carbonization and graphenization. After a second exposure of the flashlight with prior irradiation conditions, the overall sheet resistance of the FPG was additionally reduced via further FPG formation reaction followed by possible graphenization, achieving 31.37% improvement in electrical performance (sheet resistance of  $\sim 10.5 \Omega \text{ sq}^{-1}$  at 22  $\text{J}/\text{cm}^2$ ).

Figure 3b presents the Raman spectra of the FPG produced after the first and second flashlight irradiation at an energy density of 22  $\text{J}/\text{cm}^2$ . Both FPGs exhibited D peak, G peak, and 2D peak around 1350, 1580, and 2700  $\text{cm}^{-1}$ , respectively.<sup>[45,46]</sup> Note that the 2D peak serves as an indicator of graphene formation rather than amorphous carbon or graphite oxide.<sup>[47–49]</sup> The FPG obtained after a single flash lamp process showed a relatively high Raman intensity of the D peak ( $I_D$ ) compared to the G peak ( $I_G$ ), yielding an  $I_D/I_G$  ratio of 0.57. On the other hand, the FPG produced through two consecutive flashlight irradiations exhibited a decreased  $I_D/I_G$  ratio of 0.45. Given that the  $I_D/I_G$  ratio is widely regarded as a reliable indicator of defect density in graphene-based materials, this reduction in the  $I_D/I_G$  ratio implies that the crystalline quality of the FPG improves with successive irradiation steps due to the defect healing or annihilation within the graphene



**Figure 4.** a) 3D illustration (left) and photograph (right) of screen printing process for manufacturing nanocomposite-based electrodes. b) Resistance of CNT-PDMS nanocomposite ink with various CNT concentrations. c) Storage modulus and loss modulus of 3 wt% CNT-PDMS nanocomposite ink. d) Printability of screen printed electrodes at different printing speeds. e) Viscosity of 3 wt% CNT-PDMS nanocomposite ink at different shear rates.

lattice, and structural ordering and rearrangement of the FPG material.<sup>[50]</sup> Figure 3c shows the XPS analysis results of the pristine PI and the FPGs formed through successive irradiations using a high-intensity flashlight with a fluence of  $22 \text{ J cm}^{-2}$  and a pulse width of 3 ms. In the spectrum of a PI film, distinct peaks were observed corresponding to the elemental states of carbon (C 1s at 284.5 eV), nitrogen (N 1s at 400.5 eV), and oxygen (O 1s at 532.5 eV), which were characteristic of the PI molecular structure.<sup>[51]</sup> On the other hand, the XPS data for both FPGs synthesized through the first and second flash irradiations exhibited a significant increase in carbon signal intensity, accompanied by a reduction in nitrogen and oxygen signal intensities. These spectral changes signified that the progressive transformation of the PI surface during the FPG formation process resulted in the development of conductive, carbon-enriched graphitic structures. Figure 3d displays the FT-IR spectra for the as-prepared PI and the FPGs generated by the first and second flashlight treatments. The FT-IR analysis result of the pristine PI film showed characteristic peaks in the range from

1090 to  $1776 \text{ cm}^{-1}$ , which were attributed to the C–O, C–N, and C=O bonds.<sup>[52]</sup> After the flash lamp process, these peaks were no longer observed in the FT-IR spectra because specific functional groups originally present in the PI polymer were decomposed, releasing gaseous by-products such as  $\text{CO}_2$  and  $\text{N}_2$  gases during the FPG formation process.<sup>[22,44,52]</sup>

Conventional flexible electrodes formed onto uneven surfaces have critical issues of poor step coverage/adhesion and easy breakdown.<sup>[21]</sup> To resolve these issues, fast screen printing process was applied in flexible sensor electrodes by using conductive CNT-PDMS nanocomposite ink, as shown in Figure 4a. The  $3 \times 3 \text{ cm}^2$  stainless shadow mask, which had the designed microhole patterns at the desired locations, was accurately aligned onto the prepared FPG. After pouring the CNT-PDMS nanocomposite ink at the edge of the metal mask, the blade-connected printing head moved to the end of the shadow mask at a constant speed, spreading the viscous ink with the setting thickness. Prior to the printing process, the electrical property of the nanocomposite ink was optimized various CNT filler concentrations in the PDMS matrix from 1 to 5 wt%, as shown in Figure 4b. The resistance of the nanocomposite was inversely proportional to the CNT content in the matrix, decreasing  $\sim 80 \text{ k}\Omega$  at 1 wt% to  $\sim 260 \Omega$  at 5 wt%. In particular, a huge decrease of the resistance was obtained as 94.65% between 1 and 2 wt%, showing slight change of  $420 \Omega$  under 3 wt% (the inset graph of Figure 4b). These results came from the formation of an increasing amount of 1D-structured CNT connection, implying that conductive nanocomposite with  $>3 \text{ wt}\%$  CNT is suitable for the sensor electrodes. As displayed in

Figure S12, Supporting Information, the patterns from 1 wt% nanocomposite were instantly spread as making the unwanted interconnection between two electrodes, and those from  $>4 \text{ wt}\%$  nanocomposite were broken as losing the original IDE shape. Although relatively sharp edges of the IDEs were observed in range of CNT 2–3 wt%, the nanocomposite with CNT 3 wt% was used to optimize the screen printing speed because of its low electrical resistance. Figure 4c presents the viscoelastic behavior of 3 wt% CNT-PDMS nanocomposite ink. The storage modulus ( $G'$ ) exhibits negligible change across the frequency range, indicating a stable elastic network structure within the nanocomposite ink. In contrast, the loss modulus ( $G''$ ) shows slight variations, suggesting minor energy dissipation due to viscous flow. Although the elastic behavior exhibited across the entire range is beneficial for preserving the shape after printing, it presents a drawback by hindering the ink penetration via the shadow mask pattern during the printing process. Therefore, the printing speed of the screen printing process was optimized to form the printed electrode patterns. Figure 4d shows

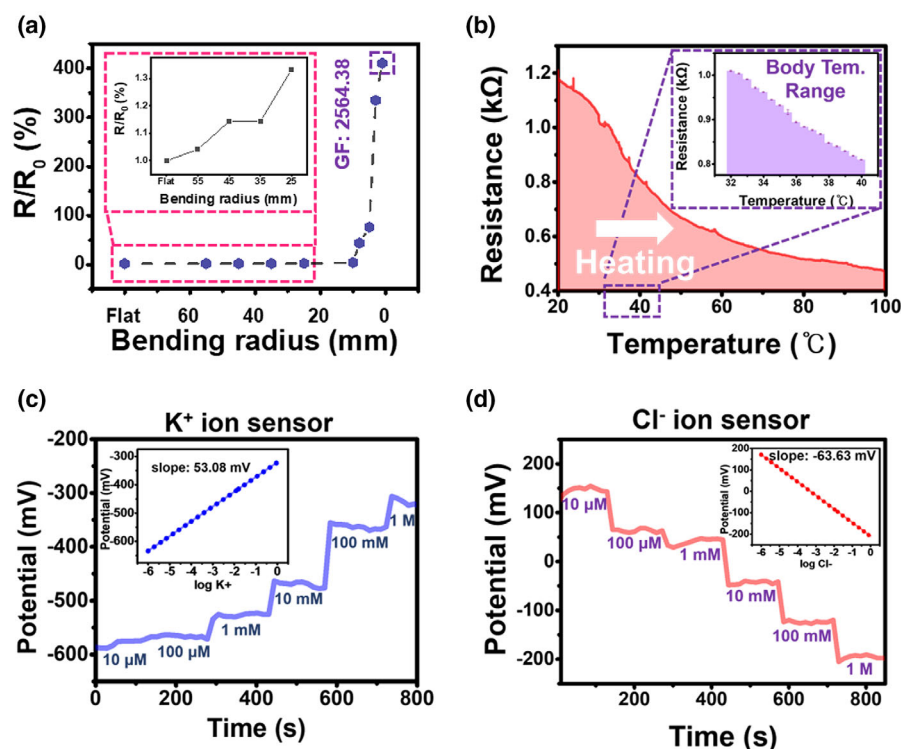


**Figure 5.** a) Resistance change of FPG-based strain sensor under bent. b) Resistance of FPG-based temperature sensor. The inset shows the resistance of the device in the range of typical human body temperature. Potentiometric response of c)  $K^+$  and d)  $Cl^-$  ion sensor in the successive concentration range of KCl solution from  $10^{-5}$  to 1 M.

printability of the 3 wt% CNT-PDMS nanocomposite ink, depending on printing speed. Printability was calculated through the following equation.

$$\text{Printability } [\%] = (A_0/A) \times 100 \quad (1)$$

$A_0$  is the printed area, and  $A$  is the area of the shadow mask pattern. At a printing speed of  $50 \text{ mm s}^{-1}$ , a printability of 99.61% was achieved, closely matching the intended electrode pattern area (red line). Furthermore, at printing speeds lower than  $50 \text{ mm s}^{-1}$ , unprinted regions were observed, indicating the reduced printability. Conversely, at printing speeds higher than  $50 \text{ mm s}^{-1}$ , printability exceeded 100% due to pattern spreading beyond the intended electrode pattern area.

Viscosity of the 3 wt% CNT-PDMS nanocomposite ink was analyzed to investigate the factors influencing printability in relation to printing speed. Figure 4e shows the viscosity change according to shear rate of the printed ink. The nanocomposite ink exhibited shear-thinning behavior, wherein its viscosity decreased with increasing shear rate. At low printing speeds, a low shear rate raised the ink viscosity for effectively penetrating the ink into the mask pattern without the unwanted spreading. In contrast, at high printing speeds, the applied high shear rate led to a low viscosity of the ink, which made it challenging to maintain the integrity of the printed pattern. Notably, the viscosity of the 3 wt% CNT-PDMS nanocomposite ink was measured to 19 Pa·s at a shear rate of  $250 \text{ s}^{-1}$  (printing speed of  $50 \text{ mm s}^{-1}$ ), falling within the optimal range of 15–20 Pa·s suitable for screen printing.<sup>[53]</sup>

Figure 5a shows the resistance changing ratio of the FPG-based flexible strain sensor at different bending curvature radii from flat to 0.1 mm. The resistance changing ratio ( $\Delta R/R_0$ ) of the FPG strain sensor, which is defined as the resistance change ( $\Delta R$ ) over the initial resistance ( $R_0$ ), increased from 1.14 to 410 according to the decrease in the bending radius. The quantified sensitivity of the strain sensor can be expressed by the following gauge factor (GF) equation:

$$GF = (\Delta R/R_0)/\epsilon \quad (2)$$

where  $\Delta R/R_0$  is the resistance changing ratio, and  $\epsilon$  is the strain rate. According to the equation, the highest GF of 2564.38 was obtained in a range of 1 mm bending radius, which was 1221 times higher value than the previously reported GO-/rGO-based hydrogel sensor.<sup>[54]</sup> These results are attributed to strain-induced minute/elaborate contact changes among micropores within the 3D FPG.<sup>[55]</sup> Figure 5b shows temperature detecting performance of the FPG-based resistive sensor from 20 to 100  $^{\circ}$ C. The developed temperature sensor exhibited the linear resistance decreasing tendency with  $9.1 \Omega ^{\circ}\text{C}^{-1}$ , especially presenting a noteworthy linearity of  $0.98 \Omega ^{\circ}\text{C}^{-1}$  under the skin temperature range

(31–40  $^{\circ}$ C). The superior sensitivity of the developed temperature sensor resulted from the 3D porous sensing layer with extremely wide surface area, promoting heat exchange and shortening the heat transfer path.<sup>[56]</sup>

Since the ion sensors measure the electrical potential from the interaction between an active layer and specific ions, a large-area active layer with the IDEs is essential to improve the device performance including sensitivity, response time, and ion interaction.<sup>[57]</sup> The 3D-structured FPG with a large surface area-to-volume ratio was adopted to fabricate flexible  $K^+$  and  $Cl^-$  ion sensors for monitoring human sweat. After coating different IDE-formed FPGs with  $K^+$  ionophore and  $Cl^-$  ionophore, potentiometric measurements were carried out with various KCl solutions (ion concentrations of 1 M, 100 mM, 10 mM, 1 mM, 100  $\mu$ M, and 10  $\mu$ M), as shown in Figure 5c,d. Flexible  $K^+$  and  $Cl^-$  ion sensors presented Nernstian behavior and adequate Nernstian response slope ( $K^+$ : 53.08 mV decade $^{-1}$ ,  $Cl^-$ : -63.63 mV decade $^{-1}$ ), showing an increasing value with cation concentration and a decreasing value with anion concentration. This behavior is consistent with the Nernst equation, which governs the electrochemical response of ion-selective electrodes. The equation predicts a positive slope for  $K^+$  cations and a negative slope for  $Cl^-$  anions, explaining the observed trends in sensor responses. Both ion sensors presented stable sensing ability of  $K^+$  and  $Cl^-$  levels in human sweat within 1 to 100 mM, especially exhibiting enhanced detection capability of 10  $\mu$ M.<sup>[58]</sup> Based on these results, it is noteworthy that our FPG is suitable for applying to sweat ion sensors due to its large surface area and efficient biomarker collection by 3D porous structure.



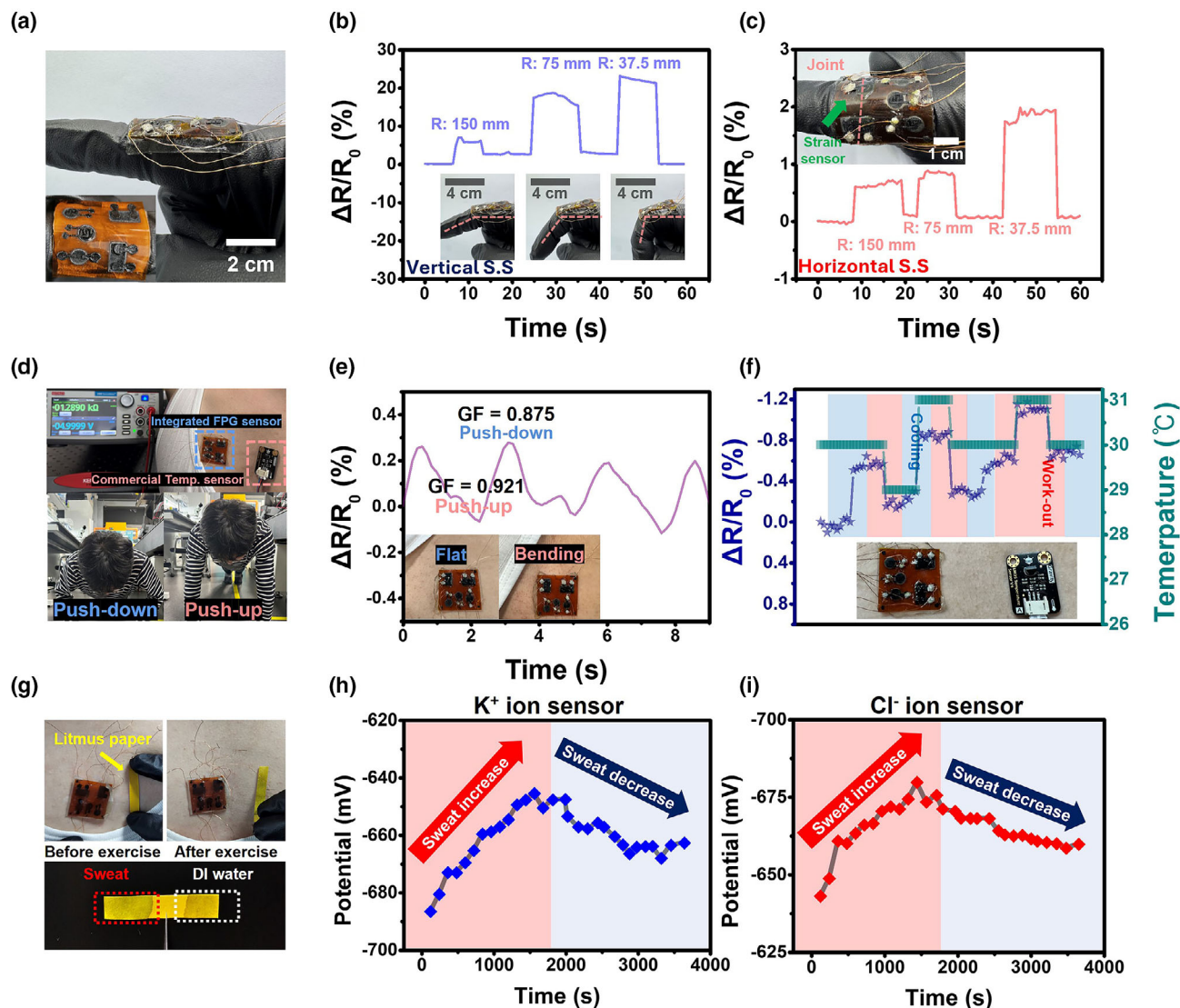


**Figure 6.** a) Optical image of FPG-based multifunctional sensor, attached to the human finger. Strain sensing characteristics under b) vertical strain and c) horizontal strain of human finger. d) Measurement setup images for monitoring body movements and skin temperature through our FPG-based multifunctional sensor. e) Resistance changes of FPG-based strain sensor by flat (push-up) and bending state (push-down) of the human scapula. f) Real-time skin temperature monitoring by FPG-based temperature sensor during workout, comparing to commercial temperature sensor. g) Photographs of the skin-attached multifunctional FPG-based sensor for sweat ion monitoring. The litmus paper color changes before and after exercise, confirming that human perspiration occurred on the skin surface during the exercise. Real-time ion sensing results of the FPG-based h)  $K^+$  and i)  $Cl^-$  ion sensors during exercise and relaxation.

Finally, the developed FPG-based devices for sensing vertical/horizontal strain, temperature and  $K^+/Cl^-$  ions were integrated on a single PI film through the large-scale FPG fabrication process. Figure 6a is a photograph of the wearable multifunctional sensor system attached to the human forearm, indicating that all nanocomposite-based electrodes were simultaneously formed on the exact location of the FPGs by the optimized screen printing process. Figure 6b,c exhibit characteristics of strain sensors with vertically and horizontally elongated shapes under various finger angles (20, 45, and 70°), respectively. When the finger bending direction was parallel to the long axial direction of the device, the maximum value of  $\Delta R/R_0$  (23.15%) was derived at a bending radius of 37.5 mm, but when they were perpendicular to each

other,  $\Delta R/R_0$  of 1.98% was obtained. Because the elongated-shape strain sensor had different magnitudes of the electrical signal depending on the bending direction, it is expected that complex movements of the human body can be more accurately monitored when the integrated sensor system is attached to the surface of the joint skin. The developed wearable sensing systems were attached to the skin surface of the human chest and scapula to confirm the applicability of body movements and temperature monitoring during workout (Figure 6d). The scapula movements during a push-up/relaxing were measured by the attached system, as shown in Figure 6e. During these push-up/down cycles, the resistance changes in our vertical and horizontal strain sensors were simultaneously measured to  $\sim 0.07$  and 0.28%, with

corresponding GF of 0.921 and 0.875. Although the small and complex movements of the human scapula occurred to the push-up exercise, our strain sensors could detect the strain change of the skin surface on the scapula. Figure 6f depicts skin temperature changes during workout, which were simultaneously measured by our temperature sensor and an existing thermometer. As the workout was implemented, the skin temperature increased from 29 to 31 °C, decreasing  $\Delta R/R_0^{-1}$  by 1.1%. The FPG-based ion sensors in the wearable system were adhered onto the human chest for comparing the change of the ion concentration before and after the workout, as presented in Figure 6g. In order to confirm the sweat ion sensitivity, the multifunctional sensor device was attached to the human chest during the exercise. Figure 6g shows the color change of litmus paper due to the perspired sweat after the workout. The color of the litmus paper turned from yellow to dark green, indicating the presence of alkaline bicarbonate ions ( $\text{HCO}_3^-$ ) in the absorbed sweat with pH 6.9. During the workout in 1800 s, each of the  $\text{K}^+$  and  $\text{Cl}^-$  sensors responded to the increased ion concentration, displaying the potential change of 39 and 36.7 mV, respectively. Despite the exercise stop, the potential of the ion sensors was slowly changed with the prolonged relaxation time, since the body perspired for hundreds of seconds by the exercise-induced heat.<sup>[59,60]</sup>

### 3. Conclusion

In summary, we demonstrated a wearable multifunctional health monitoring system using a flashlight-induced simple and fast porous graphene fabrication process. The forming conditions of the FPG were theoretically and experimentally optimized to obtain a highly quality, and defect-free film, showing a low sheet resistance of 10.5  $\Omega$ . The FPG, which was exposed under the double shots in irradiance power of 22 J cm<sup>-2</sup>, exhibited a low sheet resistance and  $I_D/I_G$  ratio compared to the single shot condition due to carbonization and graphenization. The nanocomposite-based electrode was realized to overcome the rough/uneven surface of the 3D FPG through the optimized screen printing technique with a 3 wt% of CNT-PDMS nanocomposite ink and 50 mm s<sup>-1</sup> of printing speed. The FPG-based strain and temperature sensor with superior mechanical stability exhibited high GF of 2564.38, and linear thermal response of 0.98  $\Omega$  °C<sup>-1</sup>, respectively. Enhanced detection capability in the  $\text{K}^+$  and  $\text{Cl}^-$  concentration range from 10 to 100  $\mu\text{M}$  was observed in our sweat ion sensors, which was sufficient to monitor the ion change in the human sweat. Finally, the wearable multifunctional health monitoring system with strain, temperature, and sweat ion sensors was successfully realized to analyze the human bio-signal in a single PI substrate. During the push-up exercise, our strain sensor detected the fine/complex movements of the scapula as well as temperature sensor measured the skin temperature increase from 29 to 31 °C. In addition, the changes in  $\text{K}^+$  and  $\text{Cl}^-$  ion concentration during exercise were continuously monitored by our ion sensors with a superior detection limit of 10  $\mu\text{M}$ . We believe that the FPG could become a next-generation electronic material for a various industrial field such as biomedical sensors, plant growth monitoring, and electronic skins.

### 4. Experimental Section

**Methodology for FPG generation:** Commercial PI films were precleaned in an ultrasonic bath using ethanol and de-ionized water. Photothermal pyrolysis of the

PI films was carried out under ambient conditions using a flash lamp (Model: Pulserforge 1300). The flash lamp energy density was varied in the ranges of 10–28 J cm<sup>-2</sup> at a fixed pulse duration of 3 ms. During the flash lamp irradiation process, the distance between the flash lamp and the PI substrate was maintained at 10 mm by adjusting the Z-axis moving stage.

**Photothermal simulation by finite-element method:** The temperature profile within PI during flash lamp irradiation was simulated using the finite element method with the heat transfer module of COMSOL Multiphysics 6.2. The simulation was based on the heat transfer equation:

$$\rho C \frac{\partial T}{\partial t} - \nabla \cdot (k \nabla T) = Q \quad (1)$$

where  $\rho$  denotes density,  $C$  denotes specific heat capacity,  $T$  denotes temperature,  $t$  denotes time,  $k$  denotes thermal conductivity, and  $Q$  denotes heat flux. The temperature-dependent properties ( $\rho, C, k$ ) for simulated materials (PI, air, Fe) were sourced from the COMSOL material library. The volumetric heat generation due to absorbed irradiation was derived as

$$Q(x, y) = (1-R)I_0\alpha_C e^{-\alpha_C y} \quad (2)$$

where  $R$  is the reflectance,  $I_0$  is the lamp intensity, and  $\alpha_C$  is the absorption coefficient. The reflectance and absorption coefficient of PI were determined using a UV–Visible spectroscopy (Lambda 1050, Perkin Elmer).

**Computer-aided vision image analysis:** The images were acquired from a designated data set and preprocessed to isolate the region of interest. Images were cropped to a specified size to remove unnecessary background and converted to grayscale to reduce complexity. This grayscale transformation allowed for more efficient binarization and subsequent analysis. Next, image binarization was performed to differentiate pores from the background using an adaptive thresholding method. After binarization, noise reduction was achieved by removing small white artifacts within black regions, as well as small black speckles within white regions, using connected component analysis. To analyze pore size and distribution, an Euclidean distance transform was applied to the binary image, calculating the distance from void pixels to the nearest background pixel. The maximum distance was used as a reference for pore size estimation. Pore boundaries were then dilated to enhance the measurement of major and minor axes. Key morphological properties, including pore area, and porosity, were extracted using region-based shape analysis.

**Characterization of FPG:** The surface morphology of the PI and FPG samples was observed by using field-emission SEM (JSM-IT700HR; JEOL, Akishima, Tokyo, Japan). The Raman spectra of FPGs were acquired using a Raman spectrometer (System 1000; Renishaw, Kingswood, UK) equipped with an excitation source of 514 nm laser. The chemical state and elemental composition of the samples were analyzed using XPS (Versaprobe III, ULVAC-PHI) and FT-IR (Nicolet iS50; Thermo Fisher Scientific Instrument, Waltham, MA, USA).

**Preparation of carbon nanotube-polydimethylsiloxane (CNT-PDMS) nanocomposite ink:** The multi-walled carbon nanotubes (MW-CNTs, Carbon Nanomaterial Technology Co., Ltd, CNT MR99) were dispersed in ethanol with various concentrations (0.375, 0.75, 1.125, 1.5, and 1.875 wt%). The solution was mixed by ultrasonication in 20 min to make homogeneous dispersion. Then, 2 g of PDMS base (DOW, SYLGARD 184 silicone elastomer base) was added and stirred at 80 rpm with a magnetic bar at 60 °C. After fully drying the ethanol solvent from the solution, the PDMS curing agent (DOW, SYLGARD 184 silicone elastomer curing agent) was added to follow a mixture ratio of 10:1 and vigorously mixed before the screen printing process.

**Rheological Characterization of CNT-PDMS Nanocomposite Ink:** The rheological properties of the CNT-PDMS nanocomposite inks were studied using a TA Instrument Discovery HR 30 rheometer.

**Fabrication of wearable multifunctional health monitoring systems:** After placing the synthesized FPG on the stage of the screen printer (AFA-VH; MTI Corporation, Richmond, CA, USA), the vacuum was engaged to firmly fix the FPG. A patterned metal shadow mask (3 × 3 × 0.3 mm) was accurately aligned on the fixed FPG. The CNT-PDMS nanocomposite ink was poured onto the metal mask and screen printed by moving the printing head from one end to the other with a constant speed of 50 mm s<sup>-1</sup>. The metal mask was carefully removed from the FPG, preventing the detachment or breaking of the patterned

ink. The nanocomposite-based ink was thermally cured at 80 °C for 1 h, then the desired electrodes were formed on the FPG.

**Evaluation of the sensing performances:** The multifunctional sensing system was attached to the finger, scapula, and chest of the human body to measure resistance differences by the change of strain, temperature, and ion concentration. After interconnecting Cu wires with both pads of the sensors, the electrical properties were measured by a source meter (Keithley Instruments, Keithley 2450, Cleveland, OH, USA). To confirm the resistance changes under various bending radii from flat to 0.1 mm, the devices were mounted on a conventional linear stage motor (Motorbank, LSM-NK235603, Seoul, Korea), and then bent in accordance with the exact value.

Prior to electrochemical testing of the device, the electrodes for potentiometric responses were conditioned in 1 mM KCl solution for 6 h at least, and stored at room temperature. The potential differences were analyzed by using 1 M KCl salt solution which was diluted by deionized (DI) water to make a concentration of 1 M, 100 mM, 10 mM, 1 mM, 100  $\mu$ M, and 10  $\mu$ M.

## Acknowledgements

S.J.C., C.H.K., and J.H.K. contributed equally to this work. This work was supported by the National Research Foundation of Korea (NRF) grants funded by the Ministry of Science, ICT and Future Planning (MSIT) (RS-2024-00408989, RS-2023-00278906, and RS-2023-00217661). The authors thank the Center for University-wide Research Facilities (CURF) at Jeonbuk National University for High-Resolution In Vivo Micro-Computed Tomography (Skyscan 1276, BRUKER).

## Conflict of Interest

The authors declare no conflict of interest.

## Supporting Information

Supporting Information is available from the Wiley Online Library or from the author.

## Keywords

flash-induced porous graphene, nanocomposite-based electrode, real-time biosignal monitoring, screen printing, wearable multifunctional sensor

Received: January 24, 2025  
Revised: February 5, 2025  
Published online: February 7, 2025

- [1] B. Pradhan, S. Bhattacharyya, K. Pal, *J. Healthc. Eng.* **2021**, 2021, 6632599.
- [2] K. H. Kim, H. Kim, *J. Korean Inst. Electr. Electron. Mater. Eng.* **2022**, 35, 459.
- [3] S. Chen, J. Qi, S. Fan, Z. Qiao, J. C. Yeo, C. T. Lim, *Adv. Healthc. Mater.* **2021**, 10, 2100116.
- [4] K. Kang Hyeon, K. Jeong Hyeon, K. Yu Jin, L. Han Eol, *Soft Science* **2024**, 4, 24.
- [5] A. A. Mathew, A. Chandrasekhar, S. Vivekanandan, *Nano Energy* **2021**, 80, 105566.
- [6] Y. Yamamoto, S. Harada, D. Yamamoto, W. Honda, T. Arie, S. Akita, K. Takei, *Sci. Adv.* **2016**, 2, e1601473.
- [7] R. S. Abdul Hamza, M. A. Habeeb, *Trans. Electr. Electron. Mater.* **2024**, 25, 77.
- [8] H. Zhuo, Y. Hu, Z. Chen, X. Peng, L. Liu, Q. Luo, J. Yi, C. Liu, L. Zhong, *J. Mater. Chem. A* **2019**, 7, 8092.
- [9] H. Meskher, S. B. Belhaouari, F. Sharifianjazi, *Heliyon* **2023**, 9, e21621.
- [10] C. Gui, D. Wang, J. Cao, S. Feng, *Chem. Eng. J.* **2024**, 499, 156251.
- [11] Y. Zhai, Y. Yu, K. Zhou, Z. Yun, W. Huang, H. Liu, Q. Xia, K. Dai, G. Zheng, C. Liu, C. Shen, *Chem. Eng. J.* **2020**, 382, 122985.
- [12] Y. He, L. Zhao, J. Zhang, L. Liu, H. Liu, L. Liu, *Compos. Sci. Technol.* **2020**, 200, 108419.
- [13] S. P. Muduli, M. A. Khan, P. Kale, *Trans. Electr. Electron. Mater.* **2023**, 24, 489.
- [14] H. Jahandideh, J.-R. Macairan, A. Bahmani, M. Lapointe, N. Tufenkji, *Chem. Sci.* **2022**, 13, 8924.
- [15] R. Pawlak, X. Liu, S. Ninova, P. D'Astolfo, C. Drechsel, S. Sangtarash, R. Häner, S. Decurtins, H. Sadeghi, C. J. Lambert, U. Aschauer, S. X. Liu, E. Meyer, *J. Am. Chem. Soc.* **2020**, 142, 12568.
- [16] Y. Luo, Z. Chen, Q. Li, X. Chen, *ACS Appl. Energy Mater.* **2021**, 4, 9766.
- [17] W. Song, J. Zhu, B. Gan, S. Zhao, H. Wang, C. Li, J. Wang, *Small* **2018**, 14, 1702249.
- [18] J. H. Park, H. E. Lee, C. K. Jeong, S. K. Hong, K.-I. Park, K. J. Lee, *Nano Energy* **2019**, 56, 531.
- [19] A. F. Carvalho, A. J. S. Fernandes, C. Leitão, J. Deuermeier, A. C. Marques, R. Martins, E. Fortunato, F. M. Costa, *Adv. Funct. Mater.* **2018**, 28, 1805271.
- [20] H. Wang, Z. Zhao, P. Liu, X. Guo, *npj Flexible Electronics* **2022**, 6, 26.
- [21] Y. Huang, H. Li, Z. Wang, M. Zhu, Z. Pei, Q. Xue, Y. Huang, C. Zhi, *Nano Energy* **2016**, 22, 422.
- [22] J. S. Lee, J. W. Kim, J. H. Lee, Y. K. Son, Y. B. Kim, K. Woo, C. Lee, I. D. Kim, J. Y. Seok, J. W. Yu, J. H. Park, K. J. Lee, *Nano Lett.* **2023**, 15, 191.
- [23] M. M. Hasan, M. M. Hossain, *J. Mater. Sci.* **2021**, 56, 14900.
- [24] T. Chu, S. Park, K. Fu, *Carbon Energy* **2021**, 3, 424.
- [25] X.-Y. Luo, Y. Chen, Y. Mo, *New Carbon Mater.* **2021**, 36, 49.
- [26] T. Zhang, F. Ran, *Adv. Funct. Mater.* **2021**, 31, 2010041.
- [27] X. Zhang, Z. Ju, Y. Zhu, K. Takeuchi, E. Takeuchi, A. Marschilok, G. Yu, *Adv. Energy Mater.* **2021**, 11, 2000808.
- [28] J. Oke, T.-C. Jen, *J. Mater. Res. Technol.* **2022**, 21, 2481.
- [29] Y. Kim, G. Y. Kim, I. Lee, I. Hong, J. Kim, *J. Korean Inst. Electr. Electron. Mater. Eng.* **2022**, 35, 610.
- [30] C. Bavatharani, E. Muthusankar, S. M. Wabaidur, Z. A. Alothman, K. M. Alsheetsan, M. M. Al-Anazy, D. Ragupathy, *Synth. Met.* **2021**, 271, 116609.
- [31] N. Muzaffar, M. Imran, A. M. Afzal, M. W. Iqbal, S. Mumtaz, A. Ur Rehman, T. Ejaz, M. Z. Iqbal, T. M. Almutairi, *J. Energy Storage* **2024**, 99, 113385.
- [32] A. Sankar, S. V. Chitra, M. Jayashree, M. Parthibavarmen, T. Amirthavarshini, *Diam. Relat. Mater.* **2022**, 122, 108804.
- [33] C. Sun, S. Liu, X. Shi, C. Lai, J. Liang, Y. Chen, *Chem. Eng. J.* **2020**, 381, 122641.
- [34] R. Toledano, D. Mandler, *Chem. Mater.* **2010**, 22, 3943.
- [35] C. Chen, C. Ran, Q. Yao, J. Wang, C. Guo, L. Gu, H. Han, X. Wang, L. Chao, Y. Xia, Y. Chen, *Adv. Sci.* **2023**, 10, 2303992.
- [36] R. R. Suresh, M. Lakshmanakumar, J. B. B. Arockia Jayalatha, K. S. Rajan, S. Sethuraman, U. M. Krishnan, J. B. B. Rayappan, *J. Mater. Sci.* **2021**, 56, 8951.
- [37] L. Wu, J. Qian, J. Peng, K. Wang, Z. Liu, T. Ma, Y. Zhou, G. Wang, S. Ye, *J. Mater. Sci. Mater. Electron.* **2019**, 30, 9593.
- [38] J. R. Camargo, T. A. Silva, G. A. Rivas, B. C. Janegitz, *Electrochim. Acta* **2022**, 409, 139968.
- [39] F. Arduini, L. Micheli, D. Moscone, G. Palleschi, S. Piermarini, F. Ricci, G. Volpe, *Trends Anal. Chem.* **2016**, 79, 114.
- [40] A. B. Mosbah, T. Adam, M. Mohammed, O. S. Dahham, U. Hashim, N. Z. Noriman, *IOP Conf. Ser. Mater. Sci. Eng.* **2018**, 454, 12183.
- [41] M. Inagaki, S. Harada, T. Sato, T. Nakajima, Y. Horino, K. Morita, *Carbon* **1989**, 27, 253.
- [42] M. Inagaki, L.-J. Meng, T. Ibuki, M. Sakai, Y. Hishiyama, *Carbon* **1991**, 29, 1239.



- [43] D. B. Schuepfer, F. Badaczewski, J. M. Guerra-Castro, D. M. Hofmann, C. Heiliger, B. Smarsly, P. J. Klar, *Carbon* **2020**, 161, 359.
- [44] U. Okoroanyanwu, A. Bhardwaj, J. J. Watkins, *ACS Appl. Mater. Interfaces* **2023**, 15, 13495.
- [45] J. Zhu, X. Huang, W. Song, *ACS Nano* **2021**, 15, 18708.
- [46] A. C. Ferrari, J. C. Meyer, V. Scardaci, C. Casiraghi, M. Lazzeri, F. Mauri, S. Piscanec, D. Jiang, K. S. Novoselov, S. Roth, *Phys. Rev. Lett.* **2006**, 97, 187401.
- [47] R. Murray, M. Burke, D. Iacopino, A. J. Quinn, *ACS Omega* **2021**, 6, 16736.
- [48] A. C. Ferrari, *Solid State Commun.* **2007**, 143, 47.
- [49] K. Muzyka, G. Xu, *Electroanalysis* **2022**, 34, 574.
- [50] P. Luengrojanakul, A. Klamchuen, N. Khemasiri, C. Chotsuwan, K. Charoensuk, W. Wongwiriyan, S. Rimdusit, *Mater. Res. Bull.* **2024**, 179, 112948.
- [51] D. Zeng, K. C. Yung, C. Xie, *Surf. Coat. Technol.* **2002**, 153, 210.
- [52] A. Chhetry, M. Sharifuzzaman, H. Yoon, S. Sharma, X. Xuan, J. Y. Park, *ACS Appl. Mater. Interfaces* **2019**, 11, 22531.
- [53] G. Joannou, in *The Printing Ink Manual* (Eds: R. H. Leach, C. Armstrong, J. F. Brown, M. J. Mackenzie, L. Randall, H. G. Smith), Springer US, Boston, MA **1988**, p. 481.
- [54] H. Chen, J. Huang, J. Liu, J. Gu, J. Zhu, B. Huang, J. Bai, J. Guo, X. Yang, L. Guan, *J. Mater. Chem. A* **2021**, 9, 23243.
- [55] C. G. Zhou, W. J. Sun, L. C. Jia, L. Xu, K. Dai, D. X. Yan, Z. M. Li, *ACS Appl. Mater. Interfaces* **2019**, 11, 37094.
- [56] J.-W. Lee, Y. Choi, J. Jang, S.-H. Yeom, W. Lee, B.-K. Ju, *Sensors Actuators A Phys.* **2020**, 313, 112205.
- [57] A. Kisner, R. Stockmann, M. Jansen, U. Yegin, A. Offenhäusser, L. T. Kubota, Y. Mourzina, *Biosens. Bioelectron.* **2012**, 31, 157.
- [58] Z. Sonner, E. Wilder, J. Heikenfeld, G. Kasting, F. Beyette, D. Swaile, F. Sherman, J. Joyce, J. Hagen, N. Kelley-Loughnane, *Biomechanics* **2015**, 9, 031301.
- [59] M. Parrilla, I. Ortiz-Gómez, R. Cánovas, A. Salinas-Castillo, M. Cuartero, G. N. A. Crespo, *Anal. Chem.* **2019**, 91, 8644.
- [60] D.-H. Choi, G. B. Kitchen, K. J. Stewart, P. C. Searson, *Sci. Rep.* **2020**, 10, 7699.